

COUPLED MULTI-SCALE, MULTI-PHYSICS SIMULATION FRAMEWORK FOR ALUMINIUM ELECTROLYSIS

Ingo EICK^{1*}, Wei BAI², Kristian E. EINARSRUD³, Yuqing FENG⁴, Jinsong HUA⁵, Peter J. WITT⁴

¹ Hydro Aluminium, Koblenzerstrasse 122, 41468 Neuss, Germany

² SINTEF Materials and Chemistry, 7465 Trondheim, Norway

³ Sør Trøndelag University College (HiST), 7030 Trondheim, Norway

⁴ CSIRO, Normanby Road, Clayton, VIC 3168, Australia

⁵ Institute for Energy Technology (IFE), 2027 Kjeller, Norway

*Corresponding author, E-mail address: Ingo.Eick@hydro.com

ABSTRACT

Aluminium metal production through electrolytic reduction of alumina in a cryolite bath is a complex, multi-physics, multi-scale process, containing magneto-hydrodynamics (MHD), bubble flow, thermal convection, melting and solidification phenomena based on a set of chemical reactions.

Through interactions of the different forces applied to the liquid bath combined with the different time and length scales, self-organised fluctuations occurs- In addition the MHD behaviour causes a complex metal pad profile and a series of surface waves due to the meta-stable condition of the metal / cryolite interface.

The large aspect ratio of an industrial cell, with a foot print of 20 by 4 m and at the same time having dimensions approaching just 30 mm of height for the reaction zone, prevents an integrated approach for mathematical modelling of this large degree of freedom system.

As a consequence, four different modelling approaches have been established and interlinked. Three models are used to predict details of specific physics: one to predict the electro-magnetic forces and hence the metal pad profile, a second that resolves details of the local bubble dynamics around a single anode and a third for the full cell bath flow. Results from these models are coupled to allow integration of the different phenomena into a full cell alumina distribution model. Even if several days of CPU time is needed, this modelling framework gives new insight into the process and identifies significant control parameters.

NOMENCLATURE

B	magnetic field
D	diffusion constant
F	forces
g	gravitation acceleration
J	electrical current density
P	pressure
S	source term
u	velocity
α	volume fraction
μ	viscosity
ρ	density

σ electrical conductivity

φ electrical potential

INTRODUCTION

Electrolytic aluminium metal production is a multi-scale, multi-physics process with a high degree of coupling between the pertaining non-linear forces. These coupling conditions result in a complex system, which can introduce collective behaviour, resulting in self-organized pattern (Eick & Einarsrud 2014).

To better understand the self-organized pattern and the overall process, modelling of the main dynamics contributors, the magnetic field forces and the bubble draft forces, is the obligatory approach given that the rough, hot and corrosive industrial operating conditions prevents access for easy visual inspection and measurement.

These main forces are driven by the electrical current, the main purpose of which is running the chemical reduction reaction. The changing concentrations of the species from the chemical reaction affect the bulk and surface properties, which couple back to the local Lorentz forces and bubble draft.

If complexity is about how a huge number dynamic sets of relationships between individual components generate some simple behavioural patterns, how can a modelling approach be designed to generate insight and support plotline operation?

After sketching the main process phenomena of the aluminium electrolysis process, four modelling approaches are described along with how they have been interlinked in a specific way to produce a modelling framework for predicting cell performance.

MAIN PROCESS PHENOMENA

The main or primary process phenomena are triggered by current conducted through the production system. The current drives the electrolysis reaction that then generates gas bubbles. These bubbles and the establishing of a magnetic field from the current are the main driving forces for the bath and metal flows.

Magnetic fields

In modern aluminium smelters, 150 – 450 electrolysis cells are connected side by side in a row up to 1.7 km long; exact number depends on the rectifier capacity which ranges between 800 – 2000V. At each cell a voltage drop of 4 – 4.5 volts occurs consisting of alumina dissociation (1.7V), various overvoltages (0.4V), solid conductors (0.6V), as well as about 1.5V for maintaining the inner heat. This huge current loop is operated with current load of 150000 – 600000 Ampere and built up out of a busbar system of large aluminium slabs. For geometrical reasons this system is separated into 1-3 potrooms and generates a huge magnetic field, of up to 1 Gauss, depending on design and current load. The 15-20 mm thick steel shell of each cell will reduce and modify the magnetic field before it generates Lorentz forces on the moving liquid metal and cryolite bath inside the electrolysis cell, (Hua *et al.* 2014).

With the increased current load of the recent decades, longer and longer shells up to 30 m in length with a common width of about 4 m have been developed. So finally, the length scales from the steel shell thickness up to potroom dimensions define the active magnetic field, which is builds up in milliseconds.

Bubble flow

The system current is distributed in the cell to 20 to 48 parallel-connected anodes resulting in a typical anodic current density of 0.8 to 1.0 A cm⁻². Based on Faraday's law, the applied current controls the rate of reaction (2Al₂O₃ + 3C => 3CO₂ + 4Al) for the dissolved alumina at the carbon anode that generates CO₂ gas bubbles. Whether these bubbles are nucleating out of an oversaturated cryolite bath at the anode bottom, or a competing process is absorbing dissolved CO₂ in the anode structure that gives rise to bubbles at the surface is not fully understood. At least the nucleated bubbles, which accumulate under the anode by coalescence, will move with the bypassing bath or due to anode shape and rise around the anode. These rising bubbles displace bath at the ends and sides of the anodes that results in bath circulation within the channels and lead to large scale circulation within the entire cell (Einarsrud et al 2012c). This meso-scale process, starting with about 0.4 mm small nucleated bubbles, finally results in rising large plugs of gas with a length scale of 10-20 cm with self-organising fluctuations having frequencies of 0.2 – 2 Hz.

Bath and metal flow

Inside the electrolysis cell liquid metal and cryolite bath, operating at about 950°C, are separated into two layers of about 200 mm thick by the relatively small density difference (metal 2270 g/cm³, bath 2070 g/cm³) and surface tension of about 0.56 N/m. In the macro-scale flow domain of the full cell, Lorentz forces shape the circulating metal layer in the magnetic field, which further induces local currents and fields. Besides the magneto hydrodynamic (MHD) stirring of the metal pad, the gas bubbles cause stirring of the bath layer. Here the shape of the anode and side ledge profile are significant in affecting the established flow pattern.

Compared to the shell length, the narrow reaction zone is only 30-40 mm between the anode bottom and the wavy upper interface of the metal, called anode cathode distance (ACD), so a large range of length scales are defining the bath flow. The typical flow speed is between 10-20 cm/s resulting in a circulation time of 100 seconds along the cell

and about 10 seconds along the typical 1500 mm long anode.

Reactions

In this turbulent stirred bath, alumina particles are fed at several locations with about 0.2-1 kg per shot once a minute depending on the required consumption. Additionally to the average consumption the feeding amount is varied in a 2-3 hour cycle by about ± 10-20% for process control reasons, the so-called demand feeding. The chemical process can be split in 4 main reactions based on 6 the species (Al₂O₃, Na₂Al₂O₂F₄, Na₂Al₂OF₆, Na, NaF, AlF₃) covering the dissolution of the alumina to the accumulation of aluminium metal at the cathode.

- **Dissolution** of alumina particles into the bath through the reaction:
$$2 \text{Al}_2\text{O}_{3(\text{sol})} + 6 \text{NaF} + 2\text{AlF}_3 \xrightarrow{k1} 3 \text{Na}_2\text{Al}_2\text{O}_2\text{F}_4$$
- **Equilibrium** bath reaction:
$$3 \text{Na}_2\text{Al}_2\text{O}_2\text{F}_4^{2-} + 6 \text{NaF} + 6 \text{AlF}_3 \xrightleftharpoons{k2} 6 \text{Na}_2\text{Al}_2\text{OF}_6^{2-}$$
- **Anode** boundary layer reaction:
$$6 \text{Na}_2\text{Al}_2\text{OF}_6^{2-} + 3 \text{C} \xrightarrow{k3} 12\text{e}^- + 12 \text{AlF}_3 + 12 \text{Na}^+ + 3 \text{CO}_2$$
- **Cathode** or metal pad boundary layer reaction:
$$4 \text{AlF}_3 + 12 \text{Na}^+ + 12\text{e}^- \xrightarrow{k4} 4 \text{Al} + 12 \text{NaF}$$

The dissolution process can take several minutes depending on factors such as feeding shot size, local species concentration, temperature and flow speed in the bath (Witt *et al.* 2014). Species concentrations affect bulk properties of the bath including density, viscosity and electrical conductivity, which further influence the local anodic current and the bath flow. Additionally the species change bubble-surface conditions through surface tension and dynamic contact angle, these are back coupled to the bubble flow (Solheim *et al.*, 2015).

Performance

Cell performance is strongly reliant on a stable alumina concentration in the reaction zone below the anode. Shortage of alumina results into a parasitic reaction, with back reaction of the metal and generation of additional emissions. Well selected feeder positions and local feeding doses ensure stable cell operation and high current efficiency (Moxnes, 1999).

MODEL DESCRIPTION

1) Metal pad profile model

Equations for fluid flow

The Volume of Fluid (VOF) method is used to simulate the dynamics of a two immiscible (bath and metal) fluid system by solving a single set of momentum and continuity equations, and tracking the distribution of volume fraction of each fluid throughout the computational domain, as described by Hua *et al.* (2014). The VOF formulation is generally used to compute a time-dependent solution. The governing equations of the continuity and momentum conservation for the two-phase flow system with incompressible fluids are expressed as:

$$\nabla \cdot \mathbf{u} = 0 \quad (1)$$

$$\frac{\partial}{\partial t} (\rho \mathbf{u}) + \nabla \cdot (\rho \mathbf{u} \mathbf{u}) = -\nabla P + \nabla \cdot \left[\mu (\nabla \mathbf{u} + \nabla \mathbf{u}^T) \right] + \mathbf{F}_E + \rho \mathbf{g} \quad (2)$$

where \mathbf{u} represents the flow field, and P is the pressure. \mathbf{g} refers to the gravitational acceleration. \mathbf{F}_E represents the external body force density, such as electromagnetic force known as Lorentz force. ρ and μ are the fluid density and viscosity, respectively. For this two-fluid system, the fluid properties (ρ and μ) are calculated with fluid volume fraction weighted averaging:

$$\rho = \rho_1\alpha_1 + \rho_2\alpha_2 \quad (3)$$

$$\mu = \mu_1\alpha_1 + \mu_2\alpha_2 \quad (4)$$

where the subscripts 1 and 2 denote the primary phase and the secondary phase, respectively, and α the fluid volume fraction. The bath layer is set as the primary phase, and the metal layer as the secondary phase.

The distribution of the volume fraction for each phase and the tracking of the phase-interface are accomplished by solving the continuity equation for the volume fraction of the secondary phase (α_2):

$$\frac{\partial \alpha_2}{\partial t} + \mathbf{u} \cdot \nabla \alpha_2 = 0 \quad (5)$$

The primary-phase volume fraction (α_1) will be determined by the phase continuity constraint: $\alpha_1 = 1 - \alpha_2$. In Fluent, various numerical approaches are implemented for solving the secondary phase volume fraction equation (5). The geometric reconstruction scheme in ANSYS Fluent is adopted to maintain the interface sharpness while it is moving and deforming to the final metal pad profile.

Equations for electrical field and Lorentz force field

The Lorentz force (\mathbf{F}_E) is needed to close the governing equations for fluid flow. The electric current density \mathbf{J} is calculated from Ohm's law taking into account the induced currents caused by the moving conductive liquid with velocity \mathbf{u} in an external magnetic field \mathbf{B} :

$$\mathbf{J} = -\sigma \nabla \phi + \sigma \mathbf{u} \times \mathbf{B} \quad (6)$$

Current conservation implies that the electrical potential ϕ is obtained by solving the potential equation

$$\nabla \cdot \sigma \nabla \phi = \nabla \cdot (\sigma \mathbf{u} \times \mathbf{B}) \quad (7)$$

For simplicity, locally induced magnetic fields will be neglected in the current model.

A volume fraction weighted harmonic average method is mandatory to correctly calculate the distribution of electrical conductivity over the metal-bath interface and conserve the electric current in the numerical discretization of (6):

$$\frac{1}{\sigma} = \frac{\alpha_1}{\sigma_1} + \frac{\alpha_2}{\sigma_2} \quad (8)$$

The Lorentz force density is given as

$$\mathbf{F}_E = \mathbf{J} \times \mathbf{B}, \quad (9)$$

where \mathbf{B} in the current work is a *predefined* magnetic field mimicking that expected in a conventional cell. The calculated Lorentz force is included in the source term (\mathbf{F}_E) of the momentum equation (2).

Turbulence

To limit the complexity of the problem, the standard k- ϵ turbulence model with standard wall functions is solved to calculate the turbulent viscosity in the each phase. This will allow for easy repeatability, which is the main focus of such a benchmark.

The deficiencies of the k- ϵ turbulence model for such type of flow where recirculation and re-attachment at the boundary layer could occur, are well known (Pobe, 2000). A $k-\omega$ turbulence model would probably be a better choice, but ultimately requires an exceedingly fine meshing of the boundary layer for the current application.

Model configuration

Geometry

A rectangular box model, which has the dimensions close to real cells, is shown in Figure 1 e.g. for a small electrolysis cell with 20 anodes.

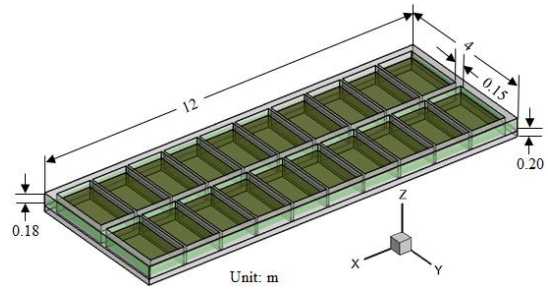


Figure 1: Geometry of the Box model for an alumina reduction cell.

It has a length of 12 m and width of 4 m. The height of metal layer is 0.2 m, and the bath layer height is 0.18 m. The distance between anode and metal-bath interface (ACD) is set to be 0.045 m. The width of central and side channels is 0.15 m, and the width of cross channels between the anodes is 0.05 m.

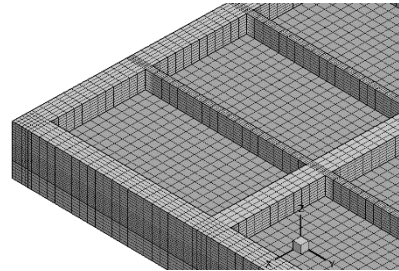


Figure 2: CFD mesh used for the numerical simulation.

The computational mesh used for the CFD analysis is shown in Figure 2. In general hexahedral cells are used. In the vertical direction, the model is divided into three zones. The top zone covers the channel height (bath above ACD). The middle zone is the interface deformation zone. It has a thickness of 0.08m that covers the ACD height and part of metal layer. The bottom zone, which has a height of 0.12 m, is meshed with six mesh grids. The CFD model contains 187,392 hexahedral cells.

It should be pointed out that the effect of side ledge profile can be taken into account to model a realistic reduction cell.

Fluid properties

In the CFD model setup, the material properties for the fluids, electrolyte and liquid aluminum are required; they are summarized in Table 1.

Table 1: Material Properties

Property	Unit	Electrolyte	Liquid Aluminum
Density	Kg m ⁻³	2070	2270
Viscosity	mPa s	1.25	2.5
Electrical conductivity	S m ⁻¹	250	3.0E6

Boundary conditions

For fluid flow, no slip boundary conditions are applied on all wall surfaces. The free surface on top of the bath is ignored by applying no slip boundary conditions as well. Standard wall functions are assumed on all solid walls for solving of the k-ε turbulence model.

As boundary for the electric potential equation, zero electric potential is set on the bottom and side of anode. Of course, in a more complete model, the anodes should be included as well and the constant potential should then be applied on top of the anodes. Electrical insulation conditions are applied on the reduction cell side walls, where the current density is set zero. Since the fluid velocity on the side walls is assumed zero, the zero-flux condition is used for the electrical potential calculation. The assumed normal current density (A m⁻²) on the cathode surface is specified explicitly by the normalized length $v=y/y_0$ along the cathode block as:

$$J_z = J_o \cdot (-2181 - 3013v^2) \quad (10)$$

with J_o as nominal current density.

The external magnetic field (mT) imposed upon both bath and metal layers inside the reduction cell is assumed as,

$$\begin{cases} B_x = B_o \cdot (-1.5 - 0.2\xi + 8.0v - 0.05\xi v) \\ B_y = B_o \cdot (-0.7 - 1.0\xi + 0.2v - 0.01\xi v) \\ B_z = B_o \cdot (-0.02 - 0.1\xi - 0.5v - 0.7\xi v) \end{cases} \quad (11)$$

based on the normalized dimensions $\xi=x/x_0$ and $v=y/y_0$ with x_0 and y_0 according to unit length and B_o nominal magnetic field. Both the prescribed normal current density J_z and the imposed magnetic field \mathbf{B} show the main characteristics of those for reduction cells, increasing current pick-up along the cathode block and the magnetic field pattern as a superposition of magnetic fields generated by the external and cell internal current carrying parts.

As in the previous benchmark (Servero *et al.*, 2008), the Ampere-Maxwell equation

$$\nabla \times \mathbf{B} = \mu_0 \mathbf{J} \quad (12)$$

is not fulfilled for the artificial magnetic field and the chosen current boundary condition for electrical current density. However, this will not lead to any inconsistencies in the simulations because equation (12) is not utilized in the model.

To take into account the consumption of anode material in aluminium electrolysis, a constant ACD is applied in the

model. Hence, the anode bottom mesh grid should be adjusted according to the heaving of metal pad. To achieve this in the current model, the ANSYS Fluent dynamics mesh model and sliding mesh interface is activated, and a UDF function is programed to move the anode bottom mesh grids accordingly.

Initial conditions

The fluid velocity inside the reduction cell is assumed to be zero. The electric potential is set zero as well. The metal/bath interface is initialized as a flat horizontal surface with a height of 0.2 m. The bath layer rests above the liquid metal layer.

Simulation schemes

In general, the numerical schemes provided by ANSYS Fluent were applied: “SIMPLE” for pressure-velocity coupling, the spatial discretization scheme “PRESTO!” for pressure, the “Geo-Reconstruct” scheme for volume fraction, and “First Order Upwind” for other equations.

A transient simulation is adopted in the modeling. “First Order Implicit” scheme is applied for the transient formulation. The time step size is set constant as 0.04s.

2) Transient mesoscale bubble model

A mesoscale modelling framework has been developed, with the aim of describing details of the bubble behaviour on the scale of a single anode. The ultimate goal is to develop a numerical laboratory from which relevant closure relations can be obtained and used in large scale models that describe global features of the full cell. Such a mesoscale model could also be used to probe details of bubble formation and evolution. The principal features of the proposed modelling framework is given in the following, while further details can be found in Einarsrud (2012a) and Einarsrud *et al.* (2012b), (2012c) and (2015).

The modelling framework is a multiscale and multi-field approach, aiming to fully resolve the behaviour of macroscopic anodic bubbles (down to a few millimetres), while phenomena occurring at smaller scales (for instance nucleation of small bubbles) is treated by means of applicable sub-grid models. The proposed modelling framework consists of five fields, as shown in Figure 3.

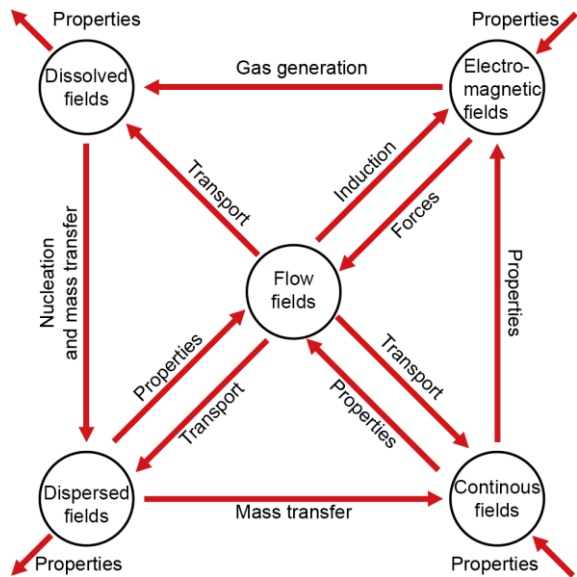


Figure 3: Overview of fields in mesoscale framework and their interactions.

Considering CO₂ as an example, it is produced on the anode surface owing to the presence of an electrical current, resulting in a field of dissolved CO₂ in close proximity of the anode, i.e. gas is on a molecular level assumed to saturate the molten bath. As concentrations approach saturation, gas bubbles nucleate and form a dispersed bubble field, which evolves by means of coalescence and mass transfer, treated by means of a discrete population balance model (PBM) in the current formulation. Upon reaching a critical volume fraction, the dispersed bubble field is converted to a continuous (fully resolved) field, treated by means of the Volume of Fluid (VOF) approach.

The outer fields depicted in Figure 3 are transported and coupled to the flow fields, while the behaviour of the electromagnetic fields (i.e. current density) and flow fields are coupled to the various material properties (e.g. electrical conductivity and viscosity) determined by the relative concentrations of dissolved species and dispersed- and continuous gas fields. Evidently, the proposed modelling framework is capable of dynamically predicting, for instance, anodic voltage oscillations, which arise due to the quasi-periodic formation and release of anodic gas bubbles.

Electromagnetic fields

The electrochemical reactions occurring in the cell are driven by an external electrical current, i.e. the principal reactions are considered to be governed by Faraday's law. The electrical current density \mathbf{J} is given in equation (6) without the second summand for induction currents, which are neglected as these typically, are small in electrolytes. The electrical potential is determined by the Poisson equation (equation 7) resulting from the requirement of current conservation. The electrical conductivity depends upon local specie- and gas concentrations and the electrical current density will thus vary both spatially and temporally, depending for instance upon gas coverage.

The electrical current density also promotes a momentum source through the Lorentz force, defined as in equation (9).

Dissolved fields

Seven separate species are considered in the current framework; Al₂O₃, NaF, AlF₃, Na₂Al₂O₂F₄, Na₂Al₂OF₆, Na⁺ and CO₂. The first six correspond to those proposed by Witt et al. (2014), aiming to represent the principal components of the bath, while CO₂ is modelled as a dissolved specie in the bath. All species (Y_i) are treated by a generic advection-diffusion equation

$$\frac{\partial \rho_b Y_i}{\partial t} + \nabla \cdot (\mathbf{u} \rho Y_i - \rho_b D_i^e \nabla Y_i) = S_i^p - S_i^c \quad (12)$$

on a mass fraction basis, where D_i^e is the effective diffusivity (including turbulent diffusion where applicable) and S_i^p and S_i^c respectively represent source and sink terms due to production and consumption of the i -th specie, for instance due to electrochemical reactions. Relevant reaction schemes and details regarding the form of the source terms can be found in Witt et al. (2014) and Einarsrud et al. (2012b).

Dispersed fields

The dispersed field is concerned with small scale bubbles, typically ranging from a diameter of 0.4 mm (observed nuclei) and up to sizes dictated by the numerical resolution.

Dispersed bubbles are modelled by means of a discrete population balance model with an exponential

discretization, allowing for tracking of bubble number densities under the influence of coalescence and mass transfer.

As the dispersed bubbles grow in size they eventually reach a size corresponding to the numerical resolution at which stage they are transferred to the continuous field, through an intermediate bubble class denoted the class, as described in Einarsrud et al. (2012b).

Continuous and flow fields

The continuous (resolved) fields in the current framework are treated by means of the Volume of Fluid (VOF) method, allowing for direct simulations of the complex bubble topology present on the anode surface. In the VOF-method, the evolution of the k -th continuous field with density ρ_k is governed by a phase fraction equation of the form

$$\frac{\partial \alpha_k \rho_k}{\partial t} + \nabla \cdot (\alpha_k \rho_k \mathbf{u}) = S_k^\alpha \quad (13)$$

where S_k^α is a source term originating from interactions with sub-grid entities, i.e. production of macroscopic gas bubbles from the dispersed elements and coalescence between large resolved bubbles and dispersed bubbles. A single flow field is shared between the phases, governed by the incompressible Navier-Stokes equations, with additional terms relating to surface tension as of the continuum surface stress model, cf. Lauffaurie et al. (1994), Lorentz-forces as of equation 2 and turbulence enhanced viscosity, as of the realizable $k - \epsilon$ -model (Shih et al., 1995).

Properties

In the current formulation large scale properties, i.e. density and viscosity are dependent upon the distribution of continuous fields, using the volume fraction of resolved gas and bath as a weighting function.

Microscopic properties, i.e. conductivity, surface tension and contact angles are dependent upon dissolved, dispersed and continuous fields, by means of applicable correlations such as for instance the Bruggeman correlation for conductivity. Details regarding relevant correlations can be found in Einarsrud et al. (2015).

Realization of mesoscale model

The proposed framework has been fully realized in ANSYS FLUENT R14.5, utilizing the user defined function and -scalar functionality to extend the existing features to the current requirements. Details regarding the implementation and recommended solver settings can be found in Einarsrud (2012a).

3) Full cell bath flow model

Computational models of the electro-magnetic fields are widely used in industry to design cells. Only recently (Feng et al., 2010b, Witt et al., 2012) have detailed computational models of the molten liquid-gas bath become available. The CFD modelling approach used in this work is to solve a steady-state model for the bath and bubble flow within a cell. Then by holding the bath flow fixed, a transient model of the alumina transport, feeding and consumption is used to predict the time varying alumina concentration in the cell.

Details of the CFD model physics, approach, validation and implementation in ANSYS/Fluent (ANSYS, 2013) have been previously documented in previous works (Feng et al.

(2010a, 2010b, 2011) Witt *et al.* (2012)). For brevity only an overview of the bath flow model is presented here.

The bath flow model describes the steady state flow of both gas and liquid phases based on a time averaged method. Key features of the bath flow model are:

- Gas and liquid flow are modelled using the Eulerian-Eulerian or two-fluid approach,
- Small-scale structures such as bubbles and turbulent structures are averaged in time and space,
- Drag from the bubbles is modelled using the Ishii and Zuber (1979) drag law,
- Turbulent effects are modelled using the $k-\varepsilon$ turbulence model with modifications for multiphase flow to include, turbulent dispersion Lopez de Bertodano (1991), bubble induced turbulence (Smith, 1998 and Olmos *et al.*, 2003) and enhanced turbulent viscosity.
- Electro-magnetic effects are included through the Lorentz force, which is calculated from magnetic field for a typical pot line and the current density, \mathbf{J} .

Electrical current model

The electrical current at the anode surface is needed for the anode reaction equation (17), for the Lorentz force and for gas generation at the anode surface. Equations (6) and (7) show the relationship between current distribution, cell voltage and bath electrical conductivity. Bath conductivity is a function of gas holdup in the ACD and alumina concentration. Thus the local voltage and current are strongly coupled to the bath flow and the alumina reduction reactions in the alumina distribution models. The electric current distribution is obtained by first solving the scalar potential equation (7) (where ϕ is the electric scalar potential or voltage) from which the current density, \mathbf{J} , is found from equation (6), neglecting the B-field.

The equations are solved as a mixture of user defined scalar equations in Fluent with the electrical conductivity calculated from the liquid conductivity calculated from species concentration (Hives *et al.*, 1994) and liquid volume fraction:

$$\sigma = \sigma_{\text{bath}} * \alpha_{\text{liquid}}^{1.5} \quad (14)$$

This current density is then used with the magnetic field calculated by Hydro from an electromagnetic model of the potroom to calculate the Lorentz Force for addition to the momentum equations.

Boundary conditions set for the electric model are that the metal pad is at a voltage of 0 Volts and that the cell current is, for example 300000 A. The approach is to set a fixed cell current while allowing the voltage and current distribution through the multiple anodes to adjust and is as follows:

1. An initial guess of the cell voltage is made and the voltage over the anode surface set,
2. Electrical conductivity is calculated based on temperature, composition, gas holdup,
3. The scalar potential equation is solved for one iteration,
4. At the end of the iteration, current through the anode base and sides is calculated.

5. An adjustment to the cell voltage is made based on the difference between the target cell current and the actual cell current.
6. Steps 2 to 6 are repeated until the model converges to a fixed cell voltage that satisfies the target cell current.

Electrical conductivity and bath viscosity are based on the species concentration and the liquid volume fraction; see Hives *et al.*, (1994) and Hertzberg *et al.* (1980).

Geometry and boundary conditions

Geometry for the single anode model was based on a Hydro Aluminium HAL300 cell and is shown in Figure 4. The full industrial cell has 30 anodes, which are included in the model together with a typical ledge profile and meshed using ANSYS/ICEM to give two million hexahedral cells.

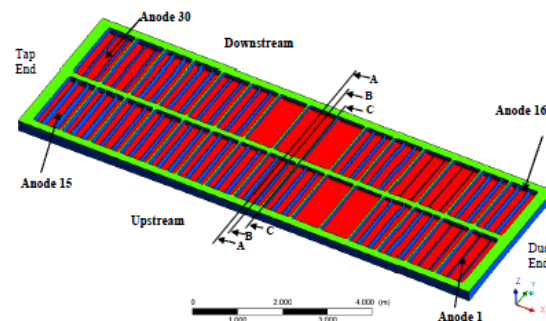


Figure 4: Full cell model geometry.

When placed in the cell the anodes had two slots that are reduced in depth as the anode is consumed, hence the slot depth for each anode depends on the age of the anode that in turn is a function of the anode changing cycle. Gas enters the model through the anode base coloured red in Figure 4. Gas leaves the domain through the free surface coloured green via a degassing boundary condition.

Bath Flow Model Implementation

The bath flow model is implemented in ANSYS/Fluent 15.0 with user-defined functions used to add and remove gas mass from the model. Also, the bubble induced turbulence, drag model, the momentum source term and fluid property dependence on temperature, species and volume fraction are implemented through user defined functions. Coupling between the electrical current model and the bath flow is very strong due to changes in gas holdup changing electrical resistance and anode surface current generating the bubble. To solve the bath flow and current iteration of the bath flow equations was performed for 10 iterations. These were turned off and solution of the potential equation performed with the iteration procedure for anode currents noted above until the potential equation converged. Solution of the bath flow was then iterated between the two sets of equations (solution of the scalar voltage potential and the bath flow equations) until the system converged.

4) Alumina distribution model

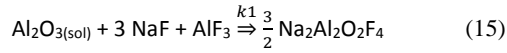
Alumina distribution within the cells is important for cell efficiency and preventing anode effects. The alumina distribution model describes the transient distribution and consumption of alumina and other chemical species within the liquid bath. Using the bath flow information and an assumption of uniform reduction, a single scalar transport equation, similar to Equation 12 has previously been used

to track the time variation of alumina within cells (Feng *et al.*, 2011). Recently a six species electrolysis model for alumina reduction was developed (Witt *et al.*, 2014) and in this work has been coupled to the bath flow model.

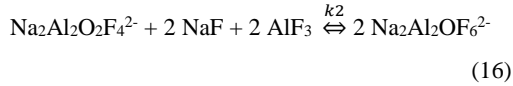
Basic electrolysis reactions

The alumina reduction process is represented by a set of four electro-chemical equations that are used to predict the distribution of six chemical species (noted earlier in the bubble model description) within the liquid bath. The key stages in reduction of alumina to aluminium metal as described by the model are:

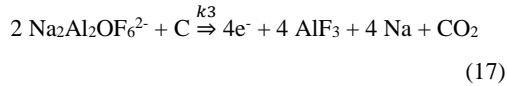
- **Feeding** of alumina to the bath surface, this can occur at various times and at a number of locations,
- **Initial breakup, mixing** and submersion of particles from the surface into the liquid bath, assumed to occur over 10 seconds,
- **Dissolution** of alumina particles into the bath through the reaction:



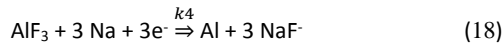
- **Equilibrium** bath reaction:



- **Anode** boundary layer reaction:



- **Cathode** or metal pad boundary layer reaction:



Reactions rates are required for equations (15) to (18).

The rate for alumina dissolution into the bath is based on the work of Frololov *et al.* (2007). By fitting two straight lines to their data, as shown in Figure 5, the following rate equation can be obtained:

$$k_1 = \max\left(0, 0.35 - \frac{0.35}{0.03} Y_{\text{Al}_2\text{O}_3\text{dis}}, 0.164 - \frac{0.164}{0.07} Y_{\text{Al}_2\text{O}_3\text{dis}}\right) \quad (19)$$

To limit the reaction in areas of low undissolved alumina the equation is modified to:

$$k_1 = (1.0 - e^{-500 Y_{\text{Al}_2\text{O}_3\text{Und}}}) * \max\left(0, 0.35 - \frac{0.35}{0.03} Y_{\text{Al}_2\text{O}_3\text{dis}}, 0.164 - \frac{0.164}{0.07} Y_{\text{Al}_2\text{O}_3\text{dis}}\right) \quad (20)$$

where $Y_{\text{Al}_2\text{O}_3\text{dis}}$ is the mass fraction of dissolved alumina in the bath and $Y_{\text{Al}_2\text{O}_3\text{Und}}$ the undissolved alumina in the bath.

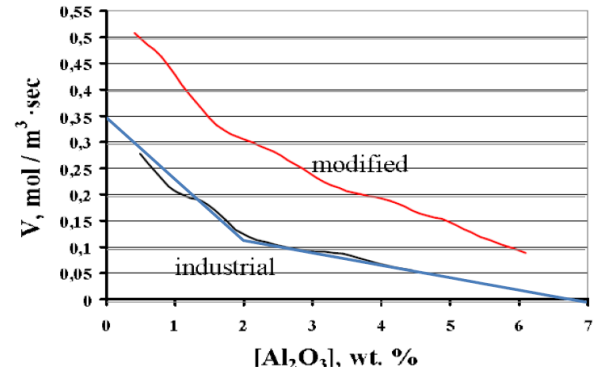


Figure 5: Dissolution rate of alumina in “modified baths” and “industrial baths” at a temperature of 960 °C from Frololov *et al.* (2007) and the model of equation (19) – blue line.

The equilibrium reaction rate is calculated assuming equilibrium of equation (16). Based on data from Solheim (1999) the equilibrium condition reported in Solheim (2013) is:

$$\frac{x_1^2}{x_2} = 11.3e^{-2.63r} \quad (21)$$

where x_1 and x_2 are the molar fractions of $\text{Na}_2\text{Al}_2\text{OF}_6$ and $\text{Na}_2\text{Al}_2\text{O}_2\text{F}_4$ respectively, and r is the molar ratio (Cryolite Ratio) of NaF and AlF_3 .

Reaction rates for the anode and cathode reactions (equations (16) and (17)) are based on the current density such that:

$$k_3 = \frac{J_{\text{Anode}} dA_a}{4F} \quad (22)$$

and

$$k_4 = \frac{J_{\text{Cathode}} dA_c}{3F} \quad (23)$$

where J_{Anode} is the current density at the anode, J_{Cathode} is the current density at the cathode, F is Faraday’s constant (96 485 [A s mol⁻¹]) and dA_a , surface area of the anode and cathode.

In cases where the current density is not solved in the model, a fixed value at the anode of 0.9 [A cm⁻²] is used and then, assuming conservation of charge, the cathode current density is:

$$J_{\text{Cathode}} = J_{\text{Anode}} \frac{A_{\text{anode}}}{A_{\text{cathode}}} \quad (24)$$

Model implementation

Transport of alumina and other chemical species is solved from transient species transport equation with convection and diffusion terms based on velocity, turbulence quantities and volume fractions from the steady state bath flow model. Source terms are used to add feeding and calculate the reaction sources and sinks terms for the species equations.

Key features of the alumina distribution model are:

- Transport of alumina is based on the steady state bath flow model,
- Alumina feeding varies in time and occurs at a number of locations,
- A fixed dissolution time of 10 seconds is assumed.

Alumina feeding occurs at different positions in the cell and at different times depending on the feeding cycle. Each feed is approximately 1 kg of alumina and feeding occurs every 80 seconds.

Initial concentrations for the mass fractions are given in Table 2 and gives a cryolite ratio of 2.2 from which the equilibrium condition for $\text{Na}_2\text{Al}_2\text{O}_6$ and $\text{Na}_2\text{Al}_2\text{O}_4$ can be determined. The model was run for a time of 20,000 seconds with 1 second time steps.

Table 2: Initial Species mass fraction in the model.

Al_2O_3	$\text{Na}_2\text{Al}_2\text{O}_4$	$\text{Na}_2\text{Al}_2\text{O}_6$	Na	NaF	AlF_3
0.025	0.044	0.084	0.070	0.420	0.382

COUPLING OF MODELS

General assumptions and connections

In complex processes, a large number of variables are involved which leads to fluctuations distributed in a Gaussian manner. Both coupling and dissipation in the system drive a system far from equilibrium and may establish a new space-time organisation (Prigogine, 1987). This new space-time organisation is an emergent property of a system where the individual component interactions result in a macroscopic behaviour, called self-organising criticality. The behaviour is further increased in complexity due to a local reversal entropy (Cilliers, 1998).

A pragmatic approach to investigate and simulate these complex processes is to separate the phenomena and try to find correlations, 1- or even 0-dimensional representations, and couple these. Especially in industrial approaches where fast or even real-time information for control and stirring is needed, this pragmatic industrial approach needs to be applied, (Zoric *et al.*, 2014).

To achieve these simplified representations a detailed physical and chemical modelling approach will be used to increase the insight and derive the effective principles. Additionally scaling of main process phenomena and their coupling behaviour can be used to structure a modelling environment for the aluminium electrolysis process.

Scales in the aluminium production process

The dimensions of the main process phenomena span over 6 decades in length and 8 decades in time preventing an integrated simulation approach covering all given phenomena with the computational working conditions in research institutes and industry. Investigating the different zones in the length/time diagram in Figure 6, indicating possible separation phenomena that can be solved in separate modelling approaches and then coupled back in to the next simulation level.

Magnetic effects are established quite fast and remain stable, based on the constant system current in the overall potlines, until the next operational impact such as metal tapping or anode changes, which occur every 24 hour. This implies that the magnetic environment can be predicted with a steady state approach with it then applied to the flow phenomena as geometrical initial condition and static magnetic field or flow boundary conditions.

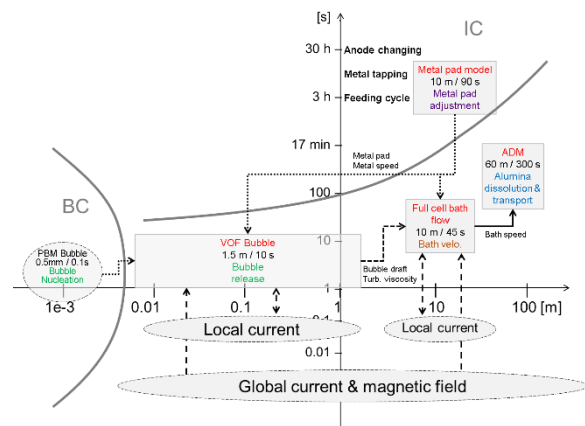


Figure 6: Location of main phenomena in length/time diagram.

The small reaction initiated gas bubbles of less than 1 mm cannot be simulated in the dimension of a 1500 mm long anode or even 30000 mm long cell, as it would require immense computer capacity to handle the millions of required elements for sufficient resolution. Therefore a mathematical model like a population balance model can be used for bubbles up to the simulation domain mesh size and then move the gas mass into volume of fluid (VOF) bubble flow, allowing the application of surface tension and wetting conditions into this transient flow behaviour.

The bubble related draft flow and turbulent viscosity can be applied in the next approach of a full cell bath flow model as time averaged volume sources, predicting the stable steady state flow pattern in the cell. Finally, this overall flow pattern can be applied in a transient alumina distribution model (ADM) for predicting the transient feeding and consumption behaviour of the electrolysis process.

Primary coupling in the aluminium production process

Figure 7 gives an overview of the different coupling mechanisms investigated here. There is a straightforward coupling from the magnetic toward the bubble part, as long as the geometrical conditions of metal pad and anode shape remain unchanged. This impact is marked with straight arrows. The impact of geometrical changes is marked with dash arrows.

Verification with lab cell and industrial cell measurement results indicate that some basic coupling mechanisms are missing in a two-phase flow without the bubble surface physics to establish typical intrinsic frequencies. This reflects the level of coupling if only the MHD and bubble induced forces are considered in the first two columns of Figure 7.

When adding the chemical species and their impact on bulk and surface properties (see dotted line in Figure 7) the coupling is extended from the bottom of the flow impact row back to the top initiating coupling loops. This is a main effect generating realistic flow and process behaviour.

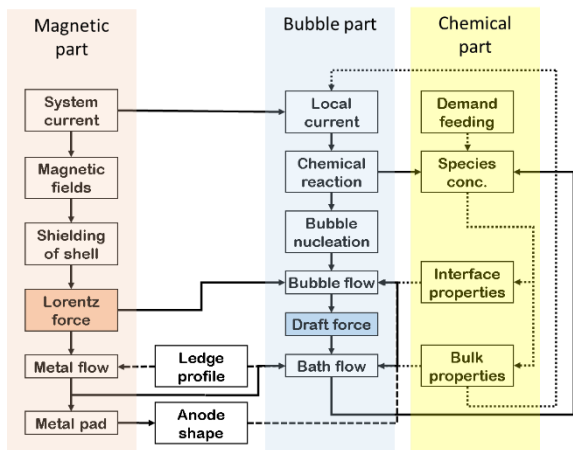


Figure 7: Primary coupling behaviour of the three process parts.

RESULTS

1) Results from metal flow model

The steadiness of the transient simulation results is estimated by averaging the transient data over a certain period of 4s. It is found that the simulations reach quasi-steady state after 240s simulation time (6000 time steps). The results presented in this paper are the simulation data at 240s or 6000 time steps.

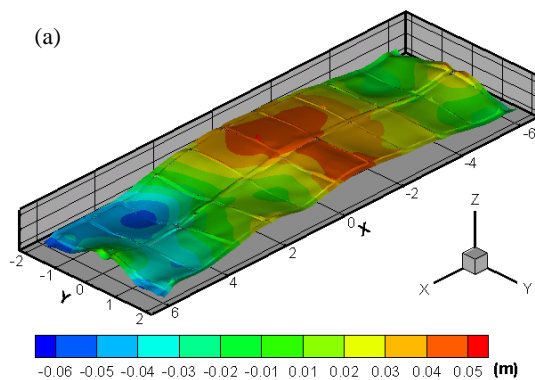


Figure 8: (a) The metal pad profile

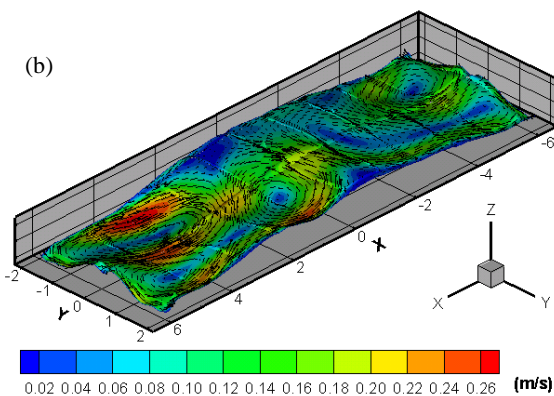


Figure 8: (b) the velocity distribution on the metal pad predicted by the simulation.

Figure 8 show the deformation of bath-metal interface at the 6000th time step predicted by the model. The metal pad heaves upward at the reduction cell center, and downward at the position near the two ends. The total metal

height difference inside the cell is about 11cm. The fluid velocity distribution on the metal pad predicted by the simulation is shown in Figure 8(b). There are several flow vortices on the metal pad. The maximum velocity in the metal layer is around 26 cm/s and the mean velocity about 14 cm s⁻¹. The metal profile and flow velocity at the metal profile are used for the boundary condition for bath flow model.

Verification of approach

Comparison of metal pad height by modelling and measurements is a quite challenging task in the harsh industrial smelting process. With the steel rod method the flow direction and speed of the bath phases can only be indirectly measured by the dissolved shape of a steel rod, submerged into the liquid part of the cell for a defined period.

The comparison between simulation results and measurements in Figure 9 is quite good, based on the simple measurement approach. More accurate measurement methods have to be developed to further increase the accuracy of the modelling approach.

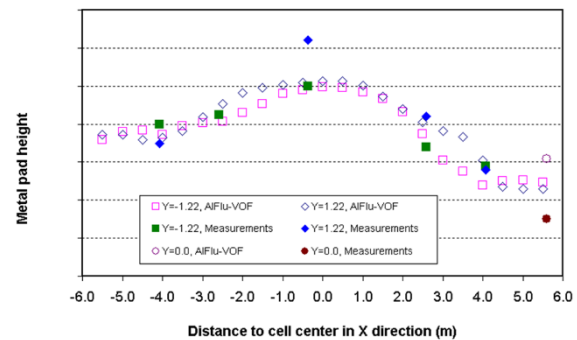


Figure 9: Comparison of metal pad height with simulation and measurements.

2) Results from mesoscale bubble model

Verification of approach

Suitable measurement techniques for the electrolyte flow pattern and species concentrations are lacking for industrial cells, owing to the harsh environments present. In order to obtain data for validation, lab scale electrolysis experiments have been performed (cf. Eick *et al.*, 2011), aiming to describe bubble induced voltage fluctuations under various operating conditions.

A subset of the experimental conditions have been simulated using the proposed approach, as described in Einarsrud *et al.* (2015). A snapshot from a simulation with current density 0.8 A/cm², 4 cm ACD and 2° anode inclination is shown in Figure 10. Qualitatively, the depicted topology of the gas bubble layer corresponds well to that observed in recent water model experiments performed by Simonsen *et al.* (2015).

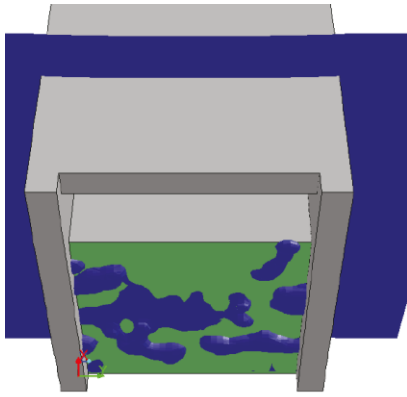


Figure 10: Typical view of simulated gas evolving anode. Gas is shown in blue, while the active anode surface is highlighted in green.

A comparison of simulated and measured voltage curves for the same conditions is shown in Figure 11. The simulated voltage signal is characterized with a frequency of 0.54 Hz and an amplitude of 97 mV, corresponding well to experimental values of 0.44 Hz and 115 mV.

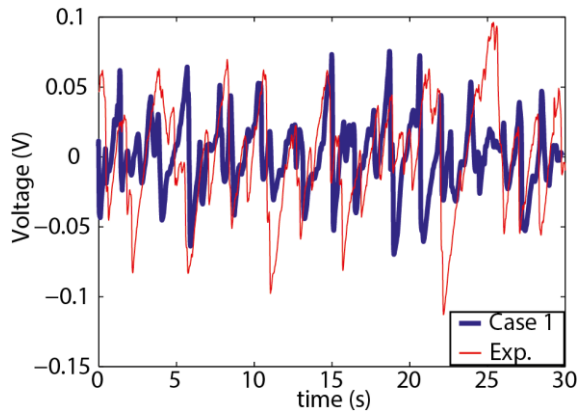


Figure 11: Simulated (blue) and experimental (red) voltage curves for current density 0.8 A m^{-2} , 4 cm ACD and 2° anode inclination.

All simulated results (amplitude (A) vs. frequency (f)) are compared to experimental results in Figure 12, with a least square fit on the form:

$$A = \frac{a}{f - b} + c, \quad (24)$$

based the *experimental* data as proposed by Wang and Taberaux (2000). Although the simulated results show somewhat higher frequencies (i.e. larger bubble velocities) and lower amplitudes (i.e. smaller bubble sizes) than the corresponding experiments, indicating that surface phenomena such as coalescence and adhesion are under predicted in the simulations, all simulated results are nevertheless within the expected range and follow the experimental trend to an acceptable level.

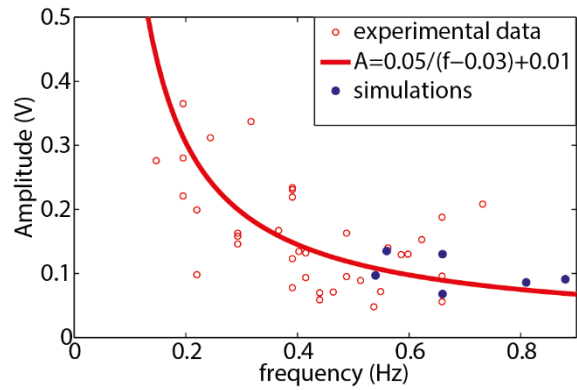


Figure 12: Summary of experiments and simulations under various operating conditions.

Single anode simulations

Typical simulation results of anode bubble flow with variation of anode tilting and current density of 0.8 and 1.0 A cm^{-2} is given in Figure 13. Anode tilting is used to represent different shapes of the metal pad profile that result in anode shaping. With increasing current density, the gas accumulation is increased as is the release frequency. With increasing the tilting angle the gas accumulation is reduced by increase release frequency.

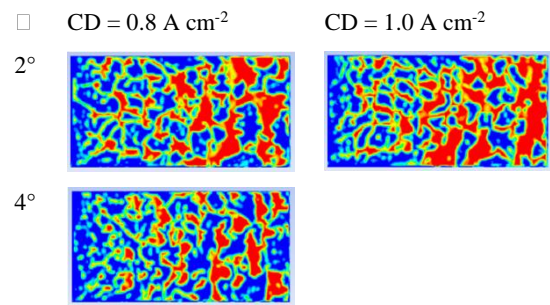


Figure 13: Gas accumulation under the anode depending on titling angle θ and current density.

This approach can be used to optimise the bubble release by different slot configurations.

3) Results from full cell bath flow model

Applying the metal pad profile and speed from the first approach and the bubble draft and turbulent viscosity from the second allow detailed MHD and bubble effects to be included into the full cell bath flow model.

Streamlines for the coupled flow field of the full simulation domain are plotted in Figure 14 and velocity vectors, as shown in Figure 15, in the centre of the anode cathode distance (ACD) on a surface parallel to the metal pad and 20 mm above the metal pad. Typical speed is about $10\text{--}20 \text{ cm s}^{-1}$ and the flow fields show that for anodes with consumed slots there is substantially stronger cross flow.

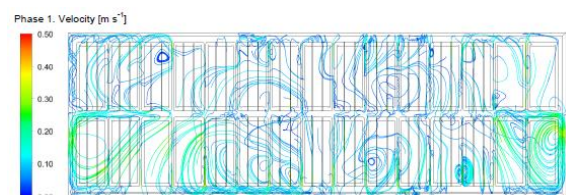


Figure 14: Streamlines for the coupled flow field of a cell on a plane through the ACD (top view).

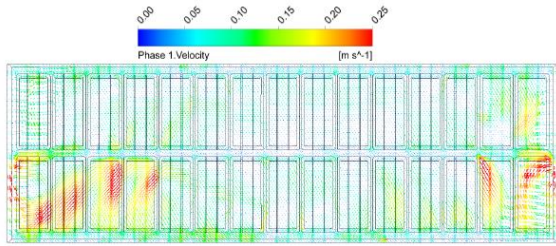


Figure 15: Velocity vectors on a plane through the ACD

Velocity vectors on a vertical plane along the centre of anodes 8 and 13 are given in Figures 16. On both outer sides toward to the side ledge, a bubble driven circulation occurs that is controlling the back flow into the ACD.

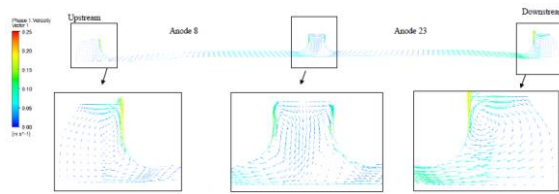


Figure 16: Bath flow across the cell width on the vertical plane A-A (Figure 4) located at the cell. Inserts show detailed flow in the side and centre channels.

4) Results from alumina distribution model

With the given bath flow pattern containing the detailed MHD and bubble effects, obtained by interlinking approaches 1 and 2 into 3, allows prediction of realistic species distribution.

Mass fractions for the undissolved alumina species are given in Figure 17, which clearly showing the feeding points and distribution based on advection and diffusion. As alumina is fed to the top of the centre channel, undissolved alumina mass fraction is highest there.

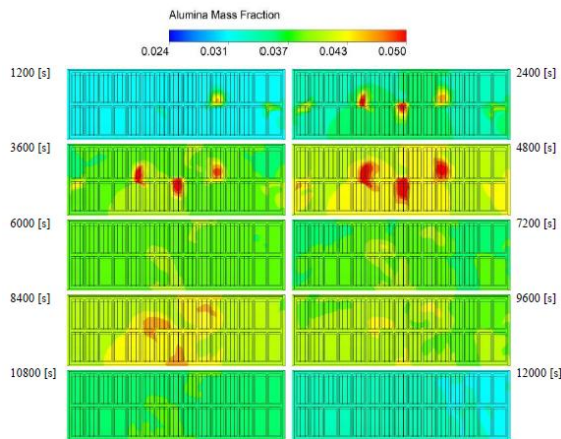


Figure 17: Undissolved alumina species during the first 12000 seconds of feeding cycle.

The model now allows investigation of the species concentration in the cell and study of the impact of the driving forces of magnetic field and bubble draft. Starvation of alumina can be identified and the feeding adjusted. This transient feeding and consumption process further gives an impression of the species fluctuations during the feeding cycle in Figure 18.

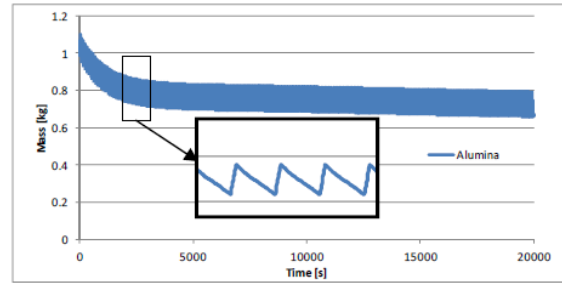


Figure 18: Change in undissolved alumina mass with time for a single anode area.

In the first 3000 seconds, the system is adjusting to an equilibrium state. Each single shot of alumina fed to the cell can be seen in the enlargement. Beside this feeding variance, the relevant oxyfluoride concentration ($\text{Na}_2\text{Al}_2\text{OF}_6$) for the anodic reaction is quite stable during the whole period.

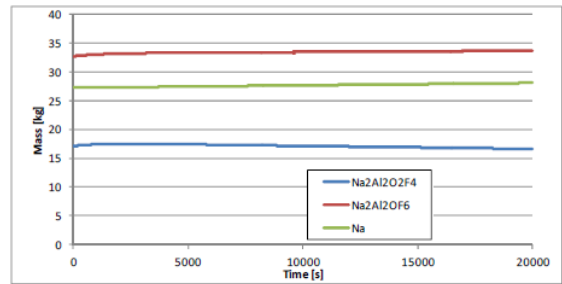


Figure 19: Change in species mass with time for a single anode area.

In addition, the species distribution and variation can be investigated as shown in Figures 20 and 21 for a single anode simulation of a corner anode in the full cell. Figure 20 shows the some selected points around a corner anode.

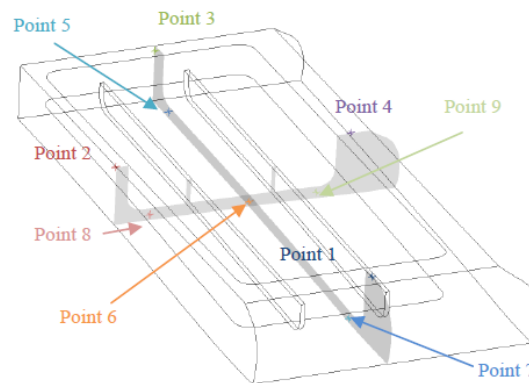


Figure 20: Locations of monitoring points for a selected corner anode simulation.

In Figure 21 the strong variation due to the feeding shot is visible, which rapidly disperses, the concentration then drops by 80% before reaching the anode centre, resulting in stable distribution.

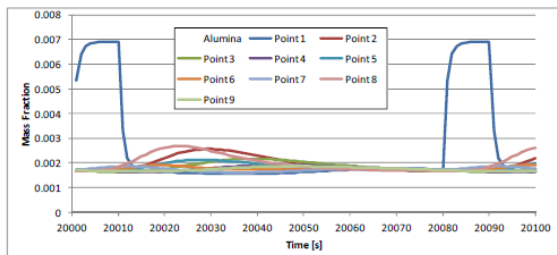


Figure 21: Change in alumina mass fraction with time at various locations in a single anode area.

CONCLUSION

A simulation environment has been developed combining four different simulation approaches to predict the aluminium electrolysis process. The MHD metal pad prediction, the multiscale and multi-field model for anodic bubble flow and the full cell bath flow approach allowing for bath chemistry and variable bath properties have been presented. Results have been verified by comparison to lab scale and industrial electrolysis experiments, showing good correspondence in the range of measurement capabilities. This simultaneously illustrates the complexity and sensitivity of detailed simulations which can be further used for defining preferred measurement locations.

Based on this approach bubble surface tension and dynamic contact angle at the rough anode surface have been indicated as significant parameters required to generate realistic bubble speed and release frequency. The bubble flow approach can be now used to predict improved slot configurations for reduced bubble overvoltage.

The reaction pathway developed for the model shows realistic behaviour based on single anode current measurements. Applications are on improved feeding strategies for reducing local and full cell anode effect and supporting selection of effective feeding positions.

The next step in the development process is the introduction of thermo-chemical effects, such as reaction enthalpy, local superheat and sludge and ledge formation and melting, see Figure 22.

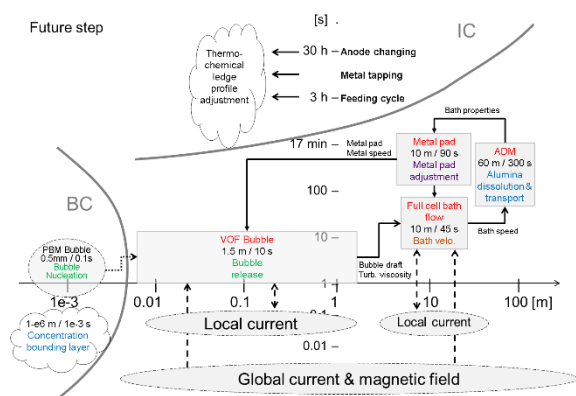


Figure 22: Impact on introduction of thermo-chemical effects.

This will further increase the coupling in the system and requires more internal iteration cycles between the sub-models. Therefore, the existing simulation environment has to be more intensively used, to develop low dimensional representations, based on the derived results.

ACKNOWLEDGMENT

The present work was supported by two projects financed by Hydro Aluminium and the Research Council of Norway. Permission to publish the results is gratefully acknowledged.

REFERENCES

- CILLIERS, P. (1998). Complexity and Postmodernism: Understanding Complex Systems, Routledge, London.
- EICK, I. et al. (2011), "Voltage and Bubble release behaviour in a laboratory cell at low anode-cathode distance", *10th AASTC, Launceston, Tasmania*.
- EICK, I and EINARSRUD, K.E., "Bubble release noise and self-organized criticality in aluminium electrolysis", *11th AASTC, Dubai 2014*
- EINARSRUD, K.E., (2012a), "A Treatise on Interpolar Transport Phenomena", *PhD Thesis 201, NTNU: Trondheim, Norway*.
- EINARSRUD, K.E. and JOHANSEN S.T., (2012b) "Modelling of Bubble Behaviour in Aluminium Reduction Cells", *Progress in Computational Fluid dynamics, 12:2*, 119-130.
- EINARSRUD, K.E., JOHANSEN, S.T. and EICK, I. (2012c), "Anodic Bubble Behaviour in Aluminium Reduction Cells", *Light Metals 2012*, 875-880.
- EINARSRUD, K.E., EICK, I., WITT, P.J., SOLHEOM, A. and FENG, Y.Q. (2015), "Impact of Variable Bath Chemistry and Wetting on Gas Bubble Flow in Aluminium Reduction Cells", *Light Metals 2015*, 649-654.
- FENG, Y.Q., COOKSEY, M. and SCHWARZ, M.P., (2010a), "CFD Modelling of alumina mixing in aluminium reduction cells", *Light Metals 2010*, 455-460.
- FENG, Y.Q., YANG, W., COOKSEY, M. and SCHWARZ, M.P., (2010b), "Development of Bubble Driven Flow CFD Model Applied for Aluminium Smelting Cells", *J. Comp. Multiphase Flows*, 2(3), 179-188.
- FENG, Y.Q., COOKSEY, M. and SCHWARZ, M.P., (2011), "CFD Modelling of alumina mixing in aluminium reduction cells", *Light Metals 2011*, 543-548.
- FROLOV, A.V., GUSEV, A.O., ZAIKOV, Y.P., KHRAMOV, A.P., SHUROV, N.I., TKACHEVA, O.Y., APISAROV, A.P. and KOVROV, V.A. (2007), "Modified alumina-cryolite bath with high electrical conductivity and dissolution rate of alumina", *Light Metals 2007*, 571-576.
- HERTZBERG T. et al (1980), "Viscosity of molten NaF-AlF₃-Al₂O₃-CaF₂ mixture; selecting and fitting models in a complex system", *Light Metals 1980*, 159-170
- HIVES J et al (1994), "Electrical conductivity of molten cryolite-based mixtures obtained with a Tube-Type cell made of Pyrolytic boron nitride", *Light Metals 1994*, 187-194
- HUA J., et al, "Revised Benchmark Problem for modelling of metal flow and metal heaving in reduction cells", *Light Metal 2014*, 691-695.
- ISHII, M. and ZUBER, N., (1979), *AIChE J.*, **25**, 843-855.

- LAFABURIE, B. et al. (1994), "Modelling Merging and Fragmentation in Multiphase Flows with SURFER", *Journal of Computational Physics*, **113:1**, 134-147.
- LOPEZ DE BERTODANO, M., (1991), *Turbulent bubbly flow in a triangular duct*, Ph.D. Thesis, Rensselaer Polytechnic Institute, New York.
- MOXNES, B., SOLHEIM, A., LIANE, M., SVINSÅS, E. and HALKJELSVIK, A., (2009), "Improved cell operation by redistribution of the alumina feeding", *Light Metals 2009*, 461-466
- PRIGOGINE I., (1987), "Exploring Complexity", *European Journal of Operational Research* 30 (1987) 97-103.
- POPE, S.B., (2000), "Turbulent Flows", Cambridge University Press.
- SEVERO, D.S., Gusberti, V., Schneider, A.F., Pinto, E.C. and Potocnik, V., (2008), "Comparison of various methods for modeling the metal-bath interface", *Light Metals 2008*: 413-418.
- OLMOS, E., GENTRIC, C. and MIDOUX, N., (2003) "Numerical description of flow regime transitions in bubble column reactors by a multiple gas phase model", *Chemical Engineering Science*, **58**, 2113-2121.
- SHIH, T.H. et al, (1995), "A new k-e Eddy-Viscosity Model for High Reynolds Number Turbulent Flows – Model Development and Validation", *Computers & Fluids*, **24**, 227-238.
- SEGATZ, M., DROSTE C. and VOLGELSANG D., (1997), "Magneto-hydrodynamic effect of anode set pattern on cell performance", *Light Metals 1997*: 429-435.
- SIMONSEN A.J. et al. (2015), "The impact of bubble-bubble interaction on anodic gas release; a water model analysis", *Light Metals 2015*, 795-800.
- SMITH, B.L., (1998) "On the modelling of bubble plumes in a liquid pool", *Applied Mathematical Modelling*, **22**, 773-797.
- SOLHEIM, A. and STERTEN, A., (1999) "Activity of Alumina in the System NaF-AlF₃-Al₂O₃ at NaF/AlF₃ Molar ratios ranging from 1.4 to 3", *Light Metals 1999*, 445-452.
- SOLHEIM, A., et al, "Wetting between carbon and cryolitic melts. Part II: Effect of bath properties and polarization", *Light Metal 2015*, 671-676
- WANG, X. and TABERAUX A.T., (2000), "Anodic phenomena - Observations of anode overvoltage and gas bubbling during aluminium electrolysis", *Light Metals 2000*, 239-247.
- WITT, P.J., FENG, Y.Q., SNOOK, G.A., EICK, I. and COOKSEY, M., et al, (2014), "A Six Chemical Species CFD Model of Alumina Reduction in a Hall-Heroult Cell", *10th Int. Conference on CFD in the Oil & Gas, Metallurgical and Process Industries, SINTEF, Trondheim, Norway, 17-19 June*.
- WITT, P.J., FENG, Y.Q., EICK, I. and SCHWARZ, M.P., (2012), "Modelling bubble flow with CFX and Fluent for aluminium reductions cells", *9th Int. Conference on CFD in the Mineral and Process Industries, CSIRO, Melbourne, Australia, 10-12 Dec*.
- ZORIC, J. et al, (2014), "On pragmatism in industrial modeling", *10th Int. Conference on CFD in the Oil & Gas, Metallurgical and Process Industries, SINTEF, Trondheim, Norway, 17-19 June*.